THE ASTROPHYSICAL JOURNAL, 469:494–507, 1996 October 1

MASS ESTIMATES OF X-RAY CLUSTERS

AUGUST E. EVRARD[1]
Physics Department, University of Michigan, Ann Arbor, MI 48109-1120; evrard@umich.edu
CHRISTOPHER A. METZLER
NASA/Fermilab Astrophysics Center, Batavia, IL 60510-0500; metzler@umich.edu
AND
JULIO F. NAVARRO[1]
Steward Observatory, University of Arizona, Tucson, AZ 85721; jnavarro@as.arizona.edu
Received 1995 September 25; accepted 1996 March 25

ABSTRACT

We use cosmological gasdynamic simulations to investigate the accuracy of galaxy cluster mass estimates based on X-ray observations. The experiments follow the formation of clusters in different cosmological models and include the effects of gravity, pressure gradients, and hydrodynamical shocks. A subset of our ensemble also allows for feedback of mass and energy from galactic winds into the intracluster medium. We find that mass estimates based on the hydrostatic, isothermal β-model are remarkably accurate when evaluated at radii where the cluster mean density is between 500 and 2500 times the critical density. At lower densities, radial temperature information becomes important. In the quoted radial regime, the distribution of the estimated-to-true mass ratio, derived from 174 artificial images constructed from the simulations, is nearly unbiased and has a standard deviation of 14%–29%. The scatter can be considerably reduced (to 8%–15%) by using an alternative mass estimator that exploits the tightness of the mass-temperature relation found in the simulations. The improvement over β-model estimates is due to the elimination of the variance contributed by the gas outer slope parameter. We discuss these findings and their implications for recent measurements of cluster baryon fractions.

Subject headings: dark matter — galaxies: clusters: general — hydrodynamics — X-rays: galaxies

1. INTRODUCTION

Estimates of the total masses of groups and clusters of galaxies have been used to infer the amount of dark matter in the universe for over 60 years. A novel technique for estimating the density parameter Ω_0 makes use of precise measurements of the visible baryonic mass fraction f_b in galaxy clusters, along with limits on the universal baryon fraction Ω_b derived from primordial nucleosynthesis. White et al. (1993) showed that cluster baryon fractions, defined as the ratio of the mass in galaxies and intracluster gas to the total cluster mass, should not differ substantially from the universal value, Ω_b/Ω_0, when determined near the outer boundary of their hydrostatic regions—roughly an Abell radius for a cluster as rich as Coma. A straightforward and unbiased estimate of the density parameter is formed by $\Omega_0 = \Omega_b/f_b$.

Recent measurements in rich clusters (Briel, Henry, & Bohringer 1992; Durret et al. 1994; David, Jones, & Forman 1995; White & Fabian 1995) and poor clusters and groups (Ponman et al. 1994; Pildis, Bregman, & Evrard 1995; Neumann & Böhringer 1995) indicate $f_b \geq 0.04\, h^{-3/2}$. (Hereafter we write Hubble's constant as 100 h km s^{-1} Mpc^{-1}.) Taken with the nucleosynthesis determination $\Omega_b \simeq 0.0125\, h^{-2}$ (Walker et al. 1991), this implies a rather small value of the density parameter, $\Omega_0 < 0.3\, h^{-1/2}$, unless primordial nucleosynthesis calculations have underestimated the universal baryon fraction by almost a factor of 3. Although there is current debate about the uncertainty in primordial nucleosynthesis determinations of Ω_b (Krauss & Kernan 1994; Copi, Schramm, & Turner 1995; Steigman 1995; Sasselov & Goldwirth 1995; Hata et al. 1996), current interpretation of the data appears to rule out the large values of Ω_b required for consistency with a universe with closure density.

These upper limits on Ω_0 are especially strong because most of the baryons in clusters are in the hot intracluster medium (ICM), a component empirically found to be more extended than the dark matter distribution (e.g., David et al. 1995). Numerical simulations show that this is a general result of hierarchical scenarios, where clusters are formed through mergers of protoclusters during which energy is transferred systematically to the gas from dark matter (Navarro & White 1993; Pearce, Thomas, & Couchman 1994). The results imply that cluster baryon fractions, measured at radii encompassing a density contrast of a few hundred, should be about 10%–20% *lower* than the universal value (Evrard 1990; Cen & Ostriker 1992).

Several solutions have been proposed to rescue $\Omega = 1$ from what has been deemed the cluster "baryon catastrophe" (Carr 1993). A low Hubble constant $H_0 \lesssim 30$ km s^{-1} Mpc^{-1} can alleviate the problem (Bartlett, Blanchard, & Silk 1995), but is in strong disagreement with recent observational estimates with favor a high value for H_0 (Freedman et al. 1994; Mould et al. 1995). A simple possibility which has not yet been explored in detail is that the binding masses inferred from X-ray observations may be systematically underestimated by a significant amount. These estimates usually rely on assumptions such as spherical symmetry, hydrostatic equilibrium for the gas, and virial equilibrium for the galaxies, none of which may be

[1] Also Institute for Theoretical Physics, University of California, Santa Barbara, CA 93106.

fully realized in practice. Clusters exhibit signatures of substructure both in the ICM (Mohr et al. 1995; Buote & Tsai 1996) and in their galaxy distributions (Dressler & Shectman 1988; Bird 1995; Crone, Evrard, & Richstone 1996), suggestive of recent mass accretion and of significant departures from equilibrium. A moderate bias in the mass estimates introduced by these effects would have important consequences for the Ω_0 limits derived by the above arguments.

Discrepancies of $\sim 50\%$ have, in fact, been reported when mass estimates of the central regions of clusters derived from X-ray observations are compared with those required to produce strong arcs by gravitational lensing of background galaxies (Miralde-Escudé & Babul 1995). Although this discrepancy could signal significant departures from hydrostatic equilibrium or support from nonthermal sources such as magnetic fields (Loeb & Mao 1994), systematic errors in the lensing mass estimates due to projection effects and substructure are more likely to be responsible for the disagreement (Bartelmann, Steinmetz, & Weiss 1995; Bartelmann 1995). In fact, at larger radii, weak gravitational lensing has also been used to measure cluster masses (Tyson, Valdes, & Wenk 1990; Bonnet, Mellier, & Fort 1994; Fahlman et al. 1994), and the small number of clusters with both X-ray and weak lensing mass estimates show no significant discrepancy between the two (Smail et al. 1995; Squires et al. 1995), although the statistical uncertainties are still large.

In this paper, we examine the accuracy of X-ray binding-mass estimates using a large number of high-resolution simulations designed to follow the nonlinear, dynamical evolution of the gravitationally coupled system of dark matter, gas, and (in one set of runs) galaxies in a variety of cosmological models. A total of 58 clusters are drawn from three separate projects using two different Lagrangian hydrodynamical codes. The models are used to generate 174 synthetic *ROSAT* X-ray images and broad-beam temperature estimates. Binding masses are then estimated for these systems in a manner analogous to that applied to observational data sets. These models are therefore ideal for understanding possible systematic effects afflicting cluster mass estimates based on X-ray observations. A recent paper by Schindler (1996) addresses the same issue using a sample of six simulations generated with very different techniques. Our results are in excellent agreement, despite the fact that the numerical methods and data analysis procedures used in the two studies differ in a number of details.

After describing briefly the numerical simulation in § 2, we begin by examining the validity of the hydrostatic and isothermal assumptions using the three-dimensional velocity and temperature profiles of simulated clusters (§ 3). We then investigate the accuracy of binding masses estimated using the simplest combination of X-ray imaging and broad-beam temperatures (§ 4). In § 5 we discuss how the tight correlation between cluster mass and X-ray temperature can be used to determine binding masses with even greater statistical accuracy. We conclude in § 6 with a brief discussion of some implications of these results.

2. NUMERICAL METHODS

2.1. *Sample Description*

We use 58 N-body/gasdynamics simulations drawn from three different projects and run with two completely independent Lagrangian codes. In all cases we use the smoothed particle hydrodynamics (SPH) technique to follow the evolution of the gas, and either a P^3M code or a tree-based N-body code to compute the gravitational interaction between particles. All the simulations assume a standard, cold dark matter (CDM) initial fluctuation spectrum with $\Gamma \equiv \Omega h = 0.5$. We neglect the radiative cooling of the gas, as well as magnetic fields as a possible source of pressure support. We take the baryon density parameter to be 0.1, and use a Hubble constant of 50 km s^{-1} Mpc^{-1} ($h = 0.5$) when scaling to physical units. Details of the models can be found in the references quoted below.

The first set consists of 28 runs from Metzler's thesis (Metzler 1995), which examines the effects of energy feedback and mass ejecta from early-type galaxies on the evolution of the ICM. The set consists of 14 clusters of different mass obtained by constraining the initial density field in cubic, periodic regions ranging from 25 to 60 Mpc (Bertschinger 1987). Each realization is run twice, once including the effects of galaxy feedback and a second, control run without feedback. We shall refer to these samples as "EJ" and "2F," respectively. All of the runs assume $\Omega = 1$. Each simulation uses a total of 65,536 particles, divided equally between gas and dark matter. A description of the feedback implementation and application to the formation of a Coma-sized cluster can be found in Metzler & Evrard (1994). The full set of runs is described in Metzler & Evrard (1996). A salient feature of the ejection runs is that they employ a rather extreme model of galactic feedback, in which early-type galaxies lose half their initial mass by winds. The EJ and 2F series are intended to define an envelope within which realistic models of feedback should lie.

The second set of runs is a sample of 24 used to investigate the X-ray cluster morphology-cosmology connection by Evrard et al. (1993) and Mohr et al. (1995). For this project eight different realizations of the initial density field were evolved within three background cosmologies in periodic cubes ranging from 30 to 60 Mpc in length. Again, 65,536 particles per run were used. The cosmological models explored were the standard CDM scenario (model "EdS"; $\sigma_8 = 0.59$, $\Omega = 1$); an unbiased, open CDM universe (model "Op2"; $\sigma_8 = 1.0$, $\Omega_0 = 0.2$, $\lambda_0 = 0$); and an unbiased, low-density universe with a flat geometry (model "Fl2"; $\sigma_8 = 1.0$, $\Omega_0 = 0.2$, $\lambda_0 = 0.8$). Here σ_8 is the rms mass fluctuation in spheres of $8\,h^{-1}$ Mpc, and Ω_0 and $\lambda_0 = \Lambda/3H_0^2$ are the present values of the density parameter and the dimensionless cosmological constant, respectively. An important aspect of this set is that the runs corresponding to each cosmology share common dynamical histories through the use of the same eight initial density fields. The benefit of this procedure is that relative differences between the final characteristics of clusters can be ascribed to the effect of the different cosmological backgrounds rather than to "cosmic scatter" in the initial density fields.

The final set consists of six models taken from Navarro, Frenk, & White (1995a; model "NFW") that were used to examine the evolution of scaling laws relating the dynamical and X-ray properties of clusters of different mass. These simulations were evolved with a code completely independent of the one used in the runs described above—a tree/SPH code described in detail in Navarro & White (1993, 1994). The six clusters were identified at $z = 0$ ($\sigma_8 = 0.63$) in the cosmological N-body simulations of Frenk et al. (1990),

and then resimulated individually at higher resolution. Each simulation has 21,296 particles, half gas and half dark matter, distributed over boxes of size 15–50 Mpc, depending on the mass of the cluster. The tidal field due to material surrounding each cluster out to 360 Mpc is treated self-consistently by coarse sampling of the surrounding matter with particles of radially increasing mass.

The ensemble of simulations span a wide range in mass and temperature, from $\sim 10^{14}$ to $3 \times 10^{15}\ M_\odot$, and from ~ 1 to 10 keV. Table 1 provides a summary, for future reference, of the runs and the notation that we use. The clusters produced in the different projects have similar spatial and mass resolution properties. The ratio between the size of a simulated cluster (as measured by the radius, r_{500}, where the mean density relative to the critical value is 500) and the gravitational softening is in the range $10 \lesssim r_{500}/\epsilon \lesssim 30$. The runs have similar numbers of particles within r_{500}, typically 5000 in each component.

2.2. *Hydrostatic, Isothermal Mass Estimates*

The typically smooth morphology of the X-ray emission from the hot intracluster medium leads naturally to the hypothesis that the gas is near equilibrium, stratified along isopotential surfaces in a mildly evolving distribution of dark matter, gas, and galaxies. The assumption of hydrostatic equilibrium—the balance between pressure gradients and gravity—for gas supported solely by thermal pressure, results in a direct measure of the binding mass $M(r)$. Assuming spherical symmetry,

$$M(r) = -\frac{kT(r)}{G\mu m_p} r\left[\frac{d\log \rho(r)}{d\log r} + \frac{d\log T(r)}{d\log r}\right], \quad (1)$$

where $\rho(r)$ and $T(r)$ are the gas density and temperature profiles, k is Boltzmann's constant, and μm_p is the mean molecular weight of the gas. In principle, all terms in the right-hand side of this equation are measurable. The main limitation is that one must deconvolve three-dimensional profiles from two-dimensional surface brightness information. This requires knowledge of, or a model for, the temperature profile $T(r)$. Since direct measurements of the temperature as a function of radius $T(r)$ (more precisely, the X-ray emission–weighted projected temperature) are still a relatively rare commodity, the common practice has been to assume that the gas is isothermal at the spatially averaged temperature T_X determined from a broad-beam spectroscopic instrument such as *EXOSAT* or *Ginga*. Preliminary *ASCA* results (Ikebe et al. 1994; Mushotzky 1994), as well as previous direct measurements (see, e.g., Watt et al. 1992) and the numerical models that we use here, generally support this assumption (see § 3.3 below).

The usual parameterization of the density profile of the ICM is based on the isothermal β-model proposed by Cavaliere & Fusco-Femiano (1976), $\rho_{ICM}(r) = \rho_0[1 + (r/r_c)^2]^{-3\beta/2}$. With this assumption, equation (1) reduces to

$$M(r) = \frac{3\beta}{G}\frac{kT_X r}{\mu m_p}\frac{(r/r_c)^2}{1+(r/r_c)^2}$$

$$= 1.13 \times 10^{15}\beta \frac{T_X}{10\ \mathrm{keV}}\frac{r}{\mathrm{Mpc}}\frac{(r/r_c)^2}{1+(r/r_c)^2} M_\odot, \quad (2)$$

assuming $\mu = 0.59$ for the second equality. For an isothermal gas, the X-ray surface brightness as a function of projected radius, $S_X(\theta)$, simply reflects the integrated emission measure and can be expressed as

$$S_X(\theta) = S_0[1 + (\theta/\theta_c)^2]^{-3\beta+1/2}. \quad (3)$$

X-ray spectroscopy provides T_X, while estimates of β and r_c are obtained from X-ray imaging.

To mimic the mass estimates derived from X-ray observations, we generate for each simulated cluster three artificial *ROSAT* images and emission-weighted temperatures T_X along the principal axes of the volume. Generating synthetic *ROSAT* images requires a choice of several parameters, including (1) the cluster redshift z, (2) the exposure time t_{exp}, and (3) the background noise level S_N. Fitting the resulting surface brightness profiles to the β-model introduces two additional parameters: (4) the background subtraction level, S_b, and (5) the minimum flux level to which the fit is performed, S_{min}. An additional choice is the energy band of the observations, which we take to be the full *ROSAT* band 0.1–2.4 keV. Because there is no obscuring galaxy in our "observations," our results are insensitive to the exact choice of the lower energy limit for the band employed. We use emission-weighted temperatures within circular apertures large enough to contain nearly all the cluster emission. Since most of the photons come from the central regions of the cluster, the estimates of T_X are rather insensitive to the aperture choice.

We use a single parameter set to construct the synthetic images of all model clusters, chosen to be representative of typical X-ray observations. We view the clusters at a redshift $z = 0.04$, image them for $t_{exp} = 7200$ s, include a Poisson background in the counts at a level of 3×10^{-4} counts s^{-1} arcmin^{-2}, subtract a mean background with exactly this value, and fit each to the β-model out to the radius at which the corrected counts reach the background level. We use emission-weighted temperatures in the same *ROSAT* band, measured within an angular scale of 16′, corresponding to a fixed metric radius of 1.04 Mpc. These parameter values are summarized in Table 2. We investigated alternative parameter sets and found that the results depended mainly on the image quality through the combination of redshift, exposure time, and assumed back-

TABLE 1

SUMMARY OF MODEL NOTATION

Label	N	Description	Reference
EJ	14	$\Omega = 1$, $\sigma_8 = 0.59$, wind ejection included	Metzler & Evrard 1994 1996
2F	14	Same as EJ without winds	Metzler & Evrard 1994, 1996
NFW.....	6	$\Omega = 1$, $\sigma_8 = 0.63$, tree/SPH code	Navarro et al. 1995a
EdS	8	$\Omega = 1$, $\sigma_8 = 0.59$, no feedback	Evrard et al. 1993
Fl2	8	$\Omega_0 = 0.2$, $\lambda_0 = 0.8$, $\sigma_8 = 1$	Evrard et al. 1993
Op2	8	$\Omega_0 = 0.2$, $\lambda_0 = 0$, $\sigma_8 = 1$	Evrard et al. 1993

TABLE 2

SYNTHETIC OBSERVATION PARAMETERS

Parameter	Value
Source redshift z	0.04
Exposure time t_{exp} (s)	7200
Background noise level S_N[a]	3×10^{-4}
Background subtraction level S_b[a]	3×10^{-4}
Minimum surface brightness in fit S_{min}[a]	3×10^{-4}

[a] Units: *ROSAT* counts s^{-1} arcmin^{-2}.

ground. The parameter choices above provide high signal-to-noise images for the majority of the sample.

For each cluster, the three images and emission-weighted temperature maps are generated and reduced to obtain the values of β, r_c, and T_X. This procedure works very well for clusters formed in cosmological models with $\Omega = 1$. However, as discussed in Mohr et al. (1995), in low-density universes the emission profiles of the cluster models are strongly peaked, resulting in unacceptably poor β-model

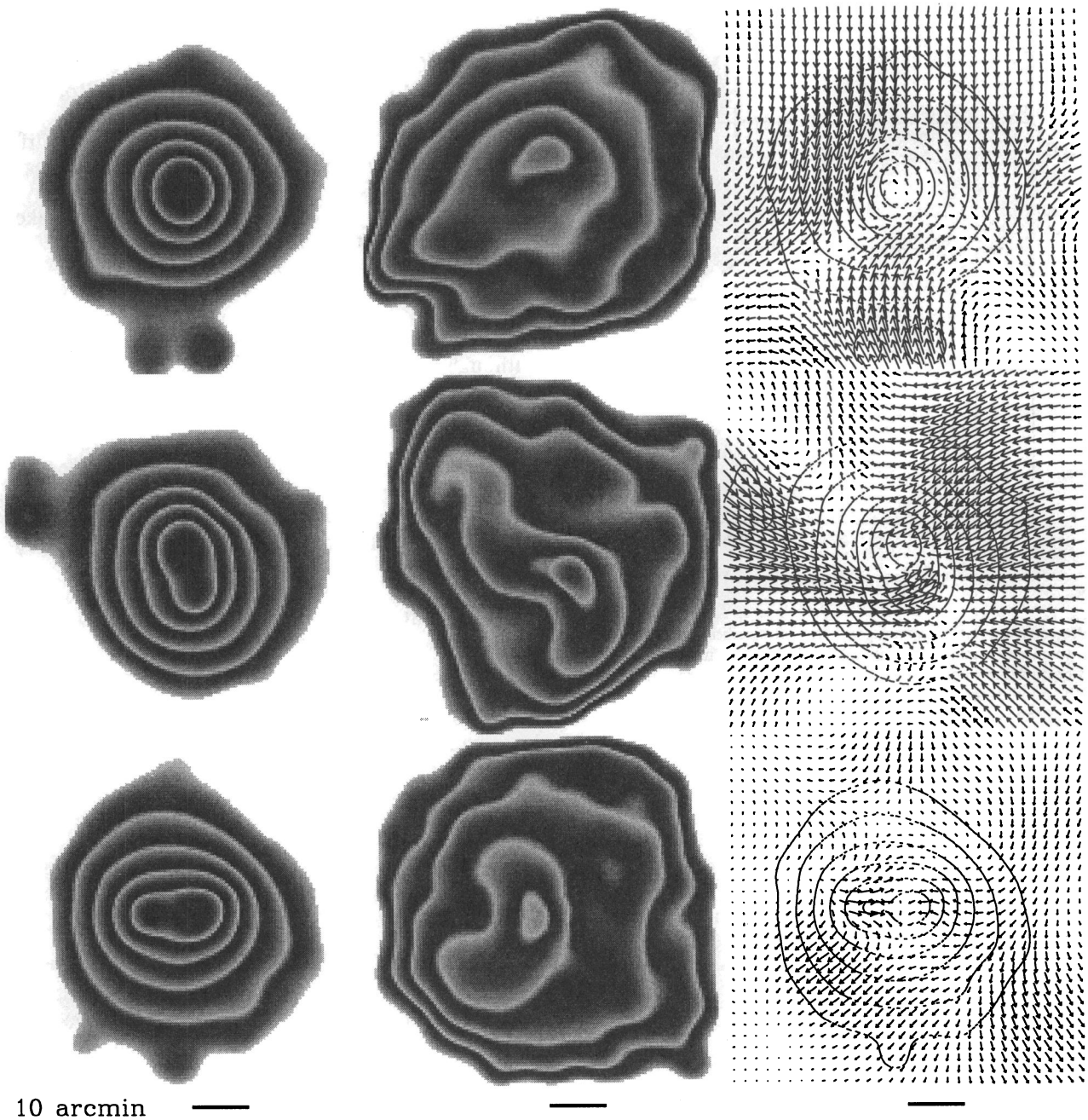

FIG. 1.—Synthetic *ROSAT* X-ray surface brightness (*left column*), emission-weighted temperature (*center column*) and emission-weighted, projected velocity field (*right column*) for three orthogonal projections of a single cluster from the EdS sample. The cluster is at an assumed redshift $z = 0.04$, and bars in the figure show a 10′ angular scale. In the gray-scale contours, the dark (or light) bands are logarithmically spaced by factors of $10^{0.6}$ in surface brightness and $10^{0.2}$ in temperature, with the third from mimimum dark band representing 10^{-3} counts s^{-1} arcmin^{-2} and 10^7 K, respectively. The velocity vectors are spaced every 2′, and scaled in such a way that 1′ = 250 km s^{-1}. The rms values of the projected velocities in the field are (*from top to bottom*) 344, 382, and 155 km s^{-1}.

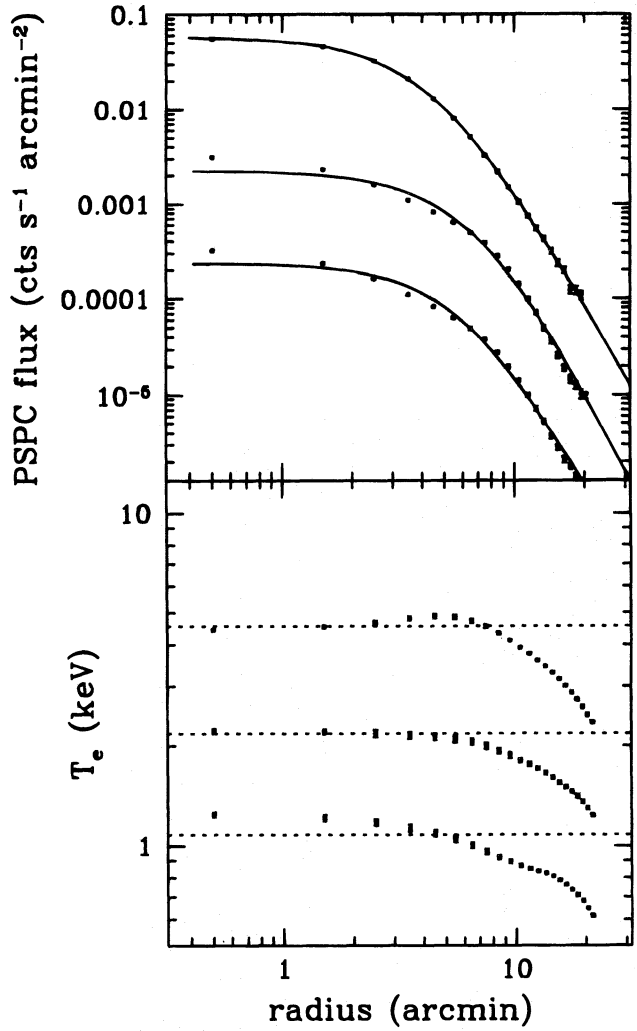

FIG. 2.—Projected azimuthally averaged X-ray surface brightness (*top*) and emission-weighted temperature (*bottom*) for the cluster shown in Fig. 1. The top to bottom lines correspond to the top to bottom projections, with data for the middle and bottom projections displaced by factors of 10 (2) and 100 (4) for the surface brightness (temperature) with respect to the top projection.

fits. In this case, we decided to excise the central regions and to fit only data outside a region of angular radius 4′, corresponding to a linear scale of 260 kpc (see Mohr et al. 1995 for details). Typical statistical uncertainties in the fitted parameters are $\lesssim 5\%$, but in a few cases the uncertainties can be as high as $\sim 40\%$. Once β, r_c, and T_X have been determined, we can estimate the binding mass as a function of radius using equation (2).

2.3. *A Particular Example*

Before examining results for the entire sample, we discuss data for a particular cluster that highlight characteristics typical of the ensemble. Figure 1 shows X-ray surface brightness and emission-weighted temperature maps, as well as the emission-weighted projected velocity field for the ICM in a cluster taken from the EdS sample. The field of view in each of the panels is 64′, corresponding to 4.2 Mpc at the assumed cluster redshift of 0.04. Two of the three projections show a bimodal central structure—the result of a recent merger involving two main sublumps with mass ratio 2.8:1. Infall patterns of the sublumps are evident in the velocity field of the middle (y-axis) projection. The temperature map shows significant variations (up to a factor of ~ 2) in temperature on scales of a few hundred kpc. The hot spots occur in regions where the gas is being compressed and mildly shocked by the interpenetrating subcluster cores. Cooler gas can be seen trailing in the wake of the substructure cores.

Several of the features of this simulated cluster, particularly the y-axis view, are reminiscent of the cluster A2256. Features in common include a bimodal central structure and spatial variations in temperature similar in morphology and amplitude (Briel et al. 1991; Miyaji et al. 1993; Briel & Henry 1994). Furthermore, an offset, extended radio halo exists in A2256 that strongly indicates the presence of a flow pattern similar to that seen in the y-axis image (Rottgering et al. 1994).

Figure 2 shows the azimuthally averaged X-ray surface brightness and emission-weighted temperature profiles for the three projections. Surface brightness profiles are scaled down successively by an order of magnitude for the sake of clarity, as are the temperature profiles by factors of 2. Values of the fitted parameters are $r_c = 294 \pm 6$, 384 ± 10, and 359 ± 9 kpc and $\beta = 0.89 \pm 0.02$, 0.85 ± 0.02, and 0.81 ± 0.02, for the three projections from top to bottom, respectively.

Although significant spatial variations in temperature are obvious in Figure 1, the radially averaged temperature profile is close to isothermal over a significant fraction of the cluster image. The temperature varies by $\lesssim 20\%$ within 10′, a region wherein the surface brightness drops by a factor of 30. The temperature drops by a factor of 2 at about 20′ from the center, but the surface brightness at this radius is already below the adopted background of 3×10^{-4} counts s^{-1} arcmin^{-2}.

From Figure 1 we learn the importance of examining spatial temperature maps directly, since a flat azimuthally average profile need not be indicative of a truly isothermal ICM. Comparison of the temperature and surface brightness maps can provide useful dynamical clues, although geometry plays an obscuring role. From the single dynamical configuration corresponding to the cluster in Figure 1, one can get, depending on projection (*from top to bottom*), (1) a fairly relaxed X-ray image with asymmetric temperature map and strong velocity gradiants; (2) a bimodal X-ray image with an S-shaped hot spot resulting from a symmetric infall pattern; and (3) a bimodal X-ray image with a peanut-shaped hot spot and a relatively modest velocity field in projection.

3. IS THE ICM HYDROSTATIC AND ISOTHERMAL?

The assumption of hydrostatic equilibrium underlies the X-ray mass-estimates method, and the assumption of isothermality greatly simplifies it. In this section, we analyze how close to hydrostatic equilibrium and isothermality the cluster models are by inspecting directly their three-dimensional velocity and temperature fields.

3.1. *The ICM Velocity Field*

Figure 3 shows the radial Mach numbers $\langle v_r \rangle / c_s$ and $\langle v_r^2 \rangle / c_s^2$ derived from the gas sound speed $c_s^2(r) = 5kT(r)/3\mu m_p$ and the first and second moments of the radial velocity field, respectively. To facilitate comparison between clusters of different sizes, the mean interior density contrast

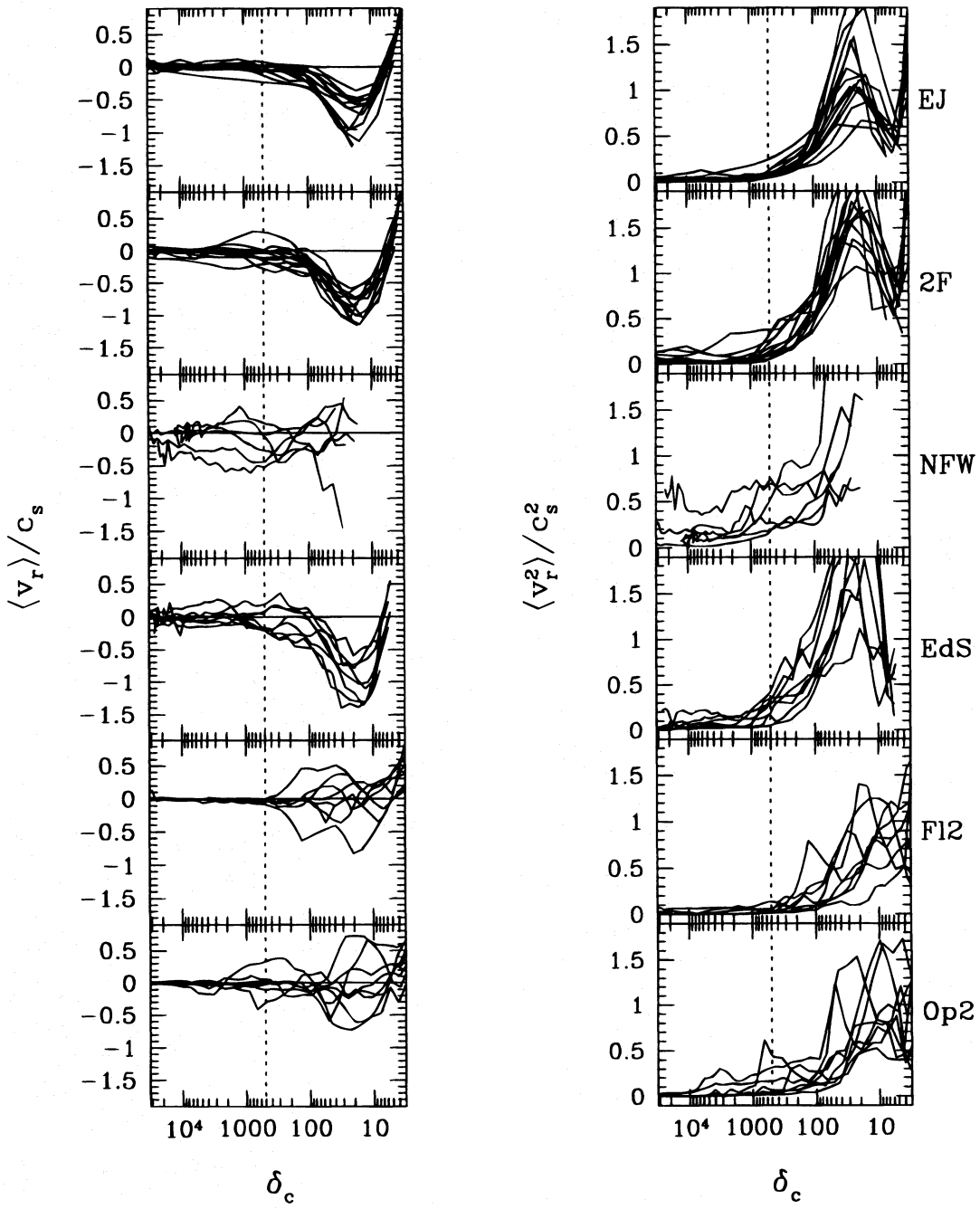

FIG. 3.—Radial Mach numbers $\langle v_r \rangle / c_s$ (*left*) and $\langle v_r^2 \rangle / c_s^2$ (*right*) derived from the gas sound speed $c_s^2(r) = 5kT(r)/3\mu m_p$ and the first and second moments of the radial velocity field for all the runs in the ensemble. All quantities are local values measured in radial shells. The overdensity δ_c is used as a radial coordinate; note the inverted axis. The dashed line shows $\delta_c = 500$, our conservative estimate for the boundary of the hydrostatic region.

$\delta_c(r) = 3M(r)/4\pi\rho_c r^3$ is used as the radial variable in the figure, reversed to reflect the correspondence with cluster radius. Note that the density contrast used here is defined with respect to the critical value for closure $\rho_c = 3H_0^2/8\pi G$ in all the models. The center of the cluster is defined as the position of the most bound dark matter particle, and velocities are calculated with respect to the mean velocity of all cluster particles linked by a standard friends-of-friends algorithm using a linking parameter 0.15 times the mean interparticle spacing. The $\Omega = 1$ runs all exhibit a common structure, with the exception of two of the NFW runs and one EdS run, which are undergoing strong mergers at $z = 0$. The Mach numbers of these systems are significantly higher than the average. The low-Ω runs have generally quieter velocity fields, as expected given their earlier formation times and, consequently, their dynamical maturity relative to clusters formed in a high-density universe.

The mean radial Mach number $\langle v_r \rangle / c_s$ has the characteristic signatures expected from gravitational infall (Gunn & Gott 1972). An outer zone of mildly supersonic infall surrounds the "virial" region of the cluster, within which the gas has been largely thermalized and is close to hydrostatic equilibrium. The infall regime is largely absent in the low-Ω models, due to the stagnated growth of linear perturbations on large scales. This, however, does not imply that there are no recent merger events in the open universe sample; at

least one Op2 cluster is experiencing an ongoing merger event at the present time.

The right-hand panels of Figure 3 provide an upper limit on the ratio of kinetic to thermal pressures for the gas. This ratio rises monotonically with radius, from values less than 10% for radii where $\delta_c > 500$ to values $\gtrsim 50\%$ at radii where $\delta_c \lesssim 100$. A few ongoing mergers are clearly recognized by the large values of the $\langle v_r^2 \rangle / c_s^2$ ratio near the center. In this case, interpreting the ratio between kinetic and thermal energy as the relative contribution of kinetic and thermal pressures to support the gas does not apply, since the systems are far from equilibrium. As the velocity field in Figure 1 indicates, nonzero values of $\langle v_r^2 \rangle$ arise during mergers from large-scale bulk motions of the gas across the face of a given radial shell rather than from a local, uniform dispersion on the shell.

From Figure 3, we derive a value $\delta_c = 500$ as a conservative estimate of the boundary between the inner, virialized region of the clusters and their recently accreted, still settling outer envelopes. Define r_{δ_c} as the radius within which the mean interior density is δ_c times the critical value. Then, within r_{500}, the hydrostatic equilibrium assumption is valid, since the gas is, on average, neither expanding nor contracting. This estimate is conservative in the sense that, in many clusters, hydrostatic balance appears to hold even at somewhat larger radii. The turnaround radius can be seen to occur at radii about a factor of 3 or 4 larger than r_{500} (for $\Omega = 1$). This is consistent with the spherical infall models of Bertschinger (1985), in which infalling gas is shocked nearly to rest at a radius about a third of the turnaround radius. Despite this nice agreement, we stress that the accretion in these three-dimensional models is far from spherically symmetric.

Table 3 gives mass-averaged values of the two radial Mach numbers measured within r_{500} for each set of runs. The mean radial Mach numbers are all quite small, typically a few percent or less, and are consistent with zero given the measured error in the mean. Again, the NFW set seems to be the most dynamically active, as can be seen from the measures of both velocity moments. Typical values of $\langle v_r^2 \rangle / c_s^2$ are $\lesssim 10\%$, indicating that the gas is hydrostatically supported by thermal pressure to this accuracy within r_{500}.

3.2. *Clustering Scaling*

As discussed above, we will use the radius r_{500} as a characteristic length scale separating the nearly hydrostatic central region of a cluster from the surrounding, recently accreting outer envelope. As shown by Navarro et al. (1995a, 1995b) and Metzler & Evrard (1966), clusters of different mass have similar structures when scaled to such a characteristic radius. This similarity, along with the equilibrium assumption validated above, implies a power-law relationship between cluster "size" and temperature:

$$T \propto \frac{M(<r_{500})}{r_{500}} \propto r_{500}^2 , \qquad (4)$$

as appropriate for systems of similar density in virial equilibrium. Figure 4 shows this relationship for the simulations, using the measured value of r_{500} and three orthogonal measures of the emission-weighted temperature T_X. Each cluster appears 3 times in this plot; the dispersion in T_X for different projections is typically quite small. Fitting the results with a power law, we find

$$r_{500}(T_X) = (2.48 \pm 0.17)\left(\frac{T_X}{10\ \mathrm{keV}}\right)^{1/2} \mathrm{Mpc} , \qquad (5)$$

where the quoted uncertainty in the intercept is given by the standard deviation of the residuals in the log space fit. The actual best-fit slope for each individual set of runs differs by less than 10% from the 0.5 exponent expected from equation (4). There are small offsets between the models. The ejection models, for example, have $\sim 6\%$ smaller r_{500} at a given temperature or, equivalently, $\sim 12\%$ higher emission-weighted temperatures for a given r_{500}, compared to the 2F runs. The slope for the EJ sample is also slightly ($\sim 10\%$) steeper than those of the nonejection samples, as expected from the differential effect of feedback, which raises the temperature of poor cluster gas proportionally more than that of rich clusters (Metzler & Evrard 1996). There is no significant difference between the NFW, 2F, and EdS data sets, indicating an encouraging agreement between the results of models run with completely independent codes for the same cosmological model.

3.3. *Temperature Profiles*

Figure 5shows the mass-weighted gas temperature, in units of T_X, as a function of the normalized radius r/r_{500} for all

TABLE 3

MEAN MACH NUMBERS WITHIN r_{500}

Sample	$\langle v_r \rangle / c_s$	$\langle v_r^2 \rangle / c_s^2$
EJ	0.001 ± 0.016	0.041 ± 0.010
2F	-0.022 ± 0.022	0.069 ± 0.018
NFW.....	-0.080 ± 0.119	0.261 ± 0.077
EdS	-0.008 ± 0.033	0.112 ± 0.019
Fl2	-0.012 ± 0.004	0.022 ± 0.009
Op2	-0.005 ± 0.014	0.045 ± 0.020

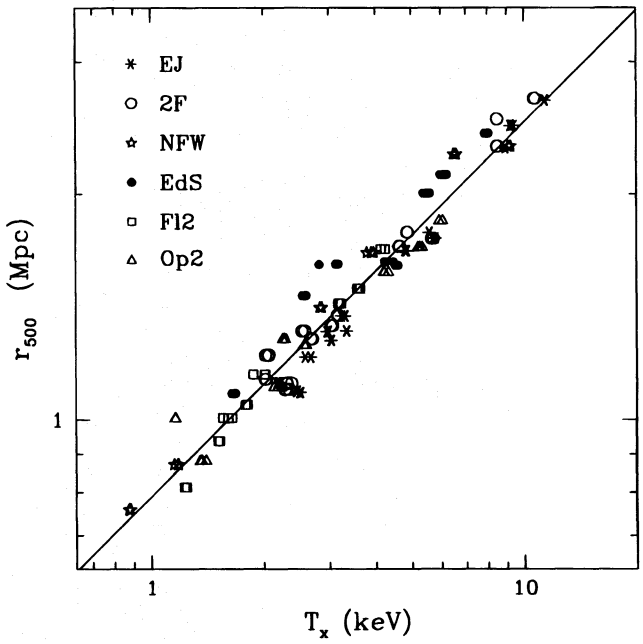

FIG. 4.—Scaling between cluster size, as measured by r_{500}, and emission-weighted temperature for all the models. Symbol types correspond to different models, as shown in the legend. The data are well fitted by eq. (5). Each model appears three times, from three orthogonal projections.

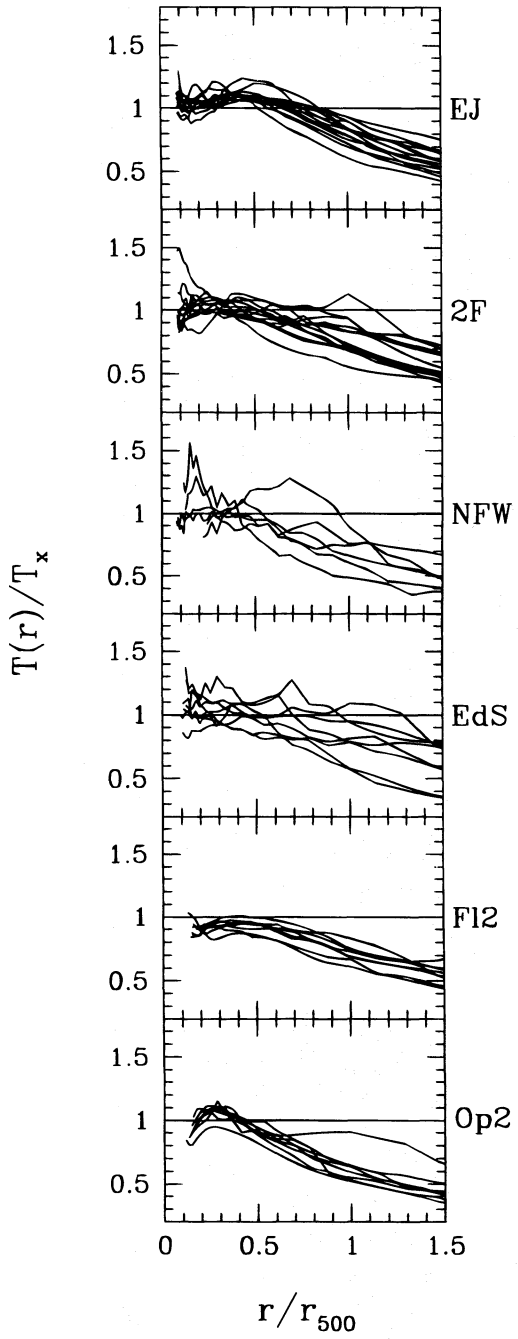

FIG. 5.—Three-dimensional temperature profiles for all the clusters in the ensemble. The temperature in radial bins is expressed in terms of the average, emission-weighted temperature T_X, and radius is normalized to the cluster size r_{500}.

runs. For $\Omega = 1$ the profiles are close to isothermal within $r_{500}/2$, and decline gently beyond that radius; the temperature at r_{500} is $\sim 20\%$ lower than at the center. In all cases, the modest drop in temperature within r_{500} is due to the fact that the density profiles of both gas and dark matter are slightly steeper than isothermal in their outer parts (Navarro et al. 1995a, 1995b). In the case of an open universe, the profiles are noticeably steeper; the temperature at r_{500} is on average a factor of 2 lower than the central value. This comes as no surprise, for the density profiles of clusters formed in low-density universes are expected to be significantly steeper than those formed in an $\Omega = 1$ cosmology (Hoffman 1988; Crone, Evrard, & Richstone 1994). Since X-ray data rarely extend significantly beyond r_{500}, an isothermal assumption should be appropriate for most observed clusters.

4. MASS ESTIMATES FROM THE β-MODEL

After constructing the synthetic *ROSAT* images as described in § 2.2, fitting the surface brightness with equation (3), and measuring the projected X-ray emission–weighted temperature, we derive estimates of the cluster binding mass as a function of radius via equation (2). Once again, in order to compare clusters of different mass (and size), we transform the radial variable into an *estimated* density contrast $\delta_c^{\rm est}$ relative to the critical density using the estimated mass $M^{\rm est}(r)$ from equation (2):

$$\delta_c^{\rm est}(r) \equiv \frac{3M^{\rm est}(r)}{4\pi\rho_c r^3} = \frac{2GM^{\rm est}(r)}{H_0^2 r^3} = \left[\frac{2\sigma(r)}{H_0 r}\right]^2, \qquad (6)$$

where $\sigma^2(r) = GM^{\rm est}(r)/2r$ is roughly the one-dimensional velocity dispersion of the cluster. For a rich cluster with $\sigma = 1000$ km s^{-1} at $r = 1\ h^{-1}$ Mpc, the estimated density constrast is $\delta_c^{\rm est} = 400$. Note that $\delta_c^{\rm est}$ depends on the combination H_0 r, and therefore it is independent of the Hubble constant, making it a useful measure of radius for observations.

Figure 6 shows the ratio between estimated and true mass as a function of the radial coordinate $\delta_c^{\rm est}$. The finite dynamic range in the simulations limits the density contrast to values $\lesssim 5000$. This figure shows that the cluster binding masses are on average quite accurately determined at overdensities between 500 and 2500. In the outer regions, where $\delta_c^{\rm est} \lesssim 200$, masses are typically overestimated because the estimated mass, assumed to increase linearly with radius, increases with radius faster than the true mass in this region. The effect is more pronounced in the low-density runs, where the cluster density profiles are steepest. Overestimates by factors up to 3 are seen in the low-density runs at $\delta_c^{\rm est} = 100$.

Figure 7 presents histograms of the estimated-to-true mass ratio at radii corresponding to $\delta_c^{\rm est} = 2500$, 500, and 100. These three values of the density contrast sample dynamically different regions and span a range comparable to that of current X-ray observations. Dashed vertical lines in the figure show $\pm 40\%$ error for reference. The trend toward overestimates at low density contrasts noted in Figure 6 is apparent in the rightmost column. The omission of the NFW runs at this contrast is technical in origin; these simulations do not extend reliably to these low overdensities.

Relatively large (a factor of ~ 2) underestimates occur in a few of the $\Omega = 1$ clusters. Three of the worst offenders arise from images of a single, strongly bimodal EdS cluster which is currently experiencing a major merger. Indeed, ongoing mergers are responsible for six of the worst underestimates at $\delta_c^{\rm est} = 500$. Synthetic *ROSAT* images of these cases are shown in Figure 8. Bold and light circles indicate the estimated and true values of r_{500}. The complex, multipeaked structure of the X-ray emission in these images is a strong signal of dynamical unrest. Although such objects would probably be rejected by observers attempting to apply an equation based on hydrostatic equilibrium, we include these cases in our analysis below, since they represent only a small fraction of the total population.

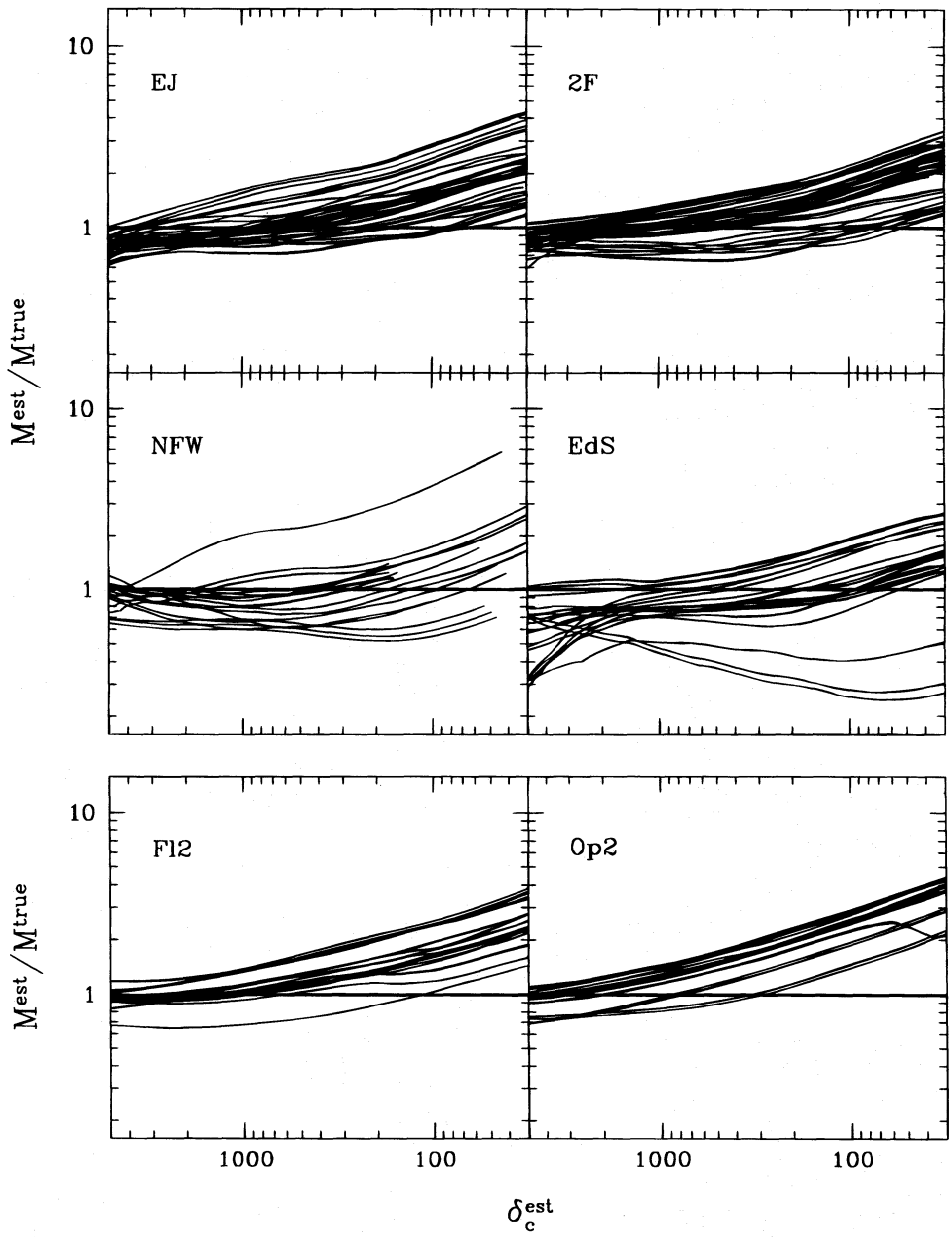

FIG. 6.—Accuracy of the β-model mass estimates as a function of the estimated density contrast δ_c^{est}, eq. (6), for the ensemble. Each model appears three times, from orthogonal projections.

The similarity between the $\Omega = 1$ sets suggests that co-adding the runs is appropriate in order to compute the ensemble statistics. Figure 9 shows the histogram of estimated-to-true mass ratios, $\mathcal{X} \equiv M^{est}/M^{true}$, evaluated at $\delta_c^{est} = 500$ for the 126 images of the combined EJ, 2F, NFW, and EdS sets. The histogram is nearly Gaussian, with mean $\bar{\mathcal{X}} = 1.02$ and standard deviation $\sigma_{\mathcal{X}} = 0.29$. At this density contrast, the β-model estimates are unbiased and have rather modest scatter. We repeated this procedure at contrasts $\delta_c^{est} = 2500$, 1000, 250, and 100. The means and standard deviations of the resulting estimated-to-true mass ratio distributions are given in Table 4 for the $\Omega = 1$ and $\Omega_0 = 0.2$ ensembles.

Values in the table reflect the trends apparent in Figures 6 and 7; the bias and the variance in the mass estimator both increase with increasing radius (i.e., toward lower density contrasts). Since the average temperature profiles decline with radius outside $\sim 0.5 r_{500}$ (Fig. 5), the biases seen at $\delta_c \lesssim 500$ are reduced by using radially averaged temperature profiles to estimates masses via equation (1) in place of an isothermal assumption. To demonstrate this explicitly, we evaluate the factor

$$\mathcal{F}(r) = \frac{-(d\ln P/d\ln r)T(r)[1 + (r_c/r)^2]}{3\beta T_x} \qquad (7)$$

for each cluster using the three-dimensional gas profiles at radii where δ_c^{est} takes on the values in Table 4. This factor is simply the ratio of the nonisothermal to isothermal mass estimates. We evaluate the mean value of $\mathcal{F}(r)$ at each δ_c^{est} for the sets of models, then apply this factor to the mean isothermal mass estimates $\mathcal{X}$. The results are shown in parenthesis in Table 4. Inclusion of radial temperature information removes the biases in the isothermal estimates. This

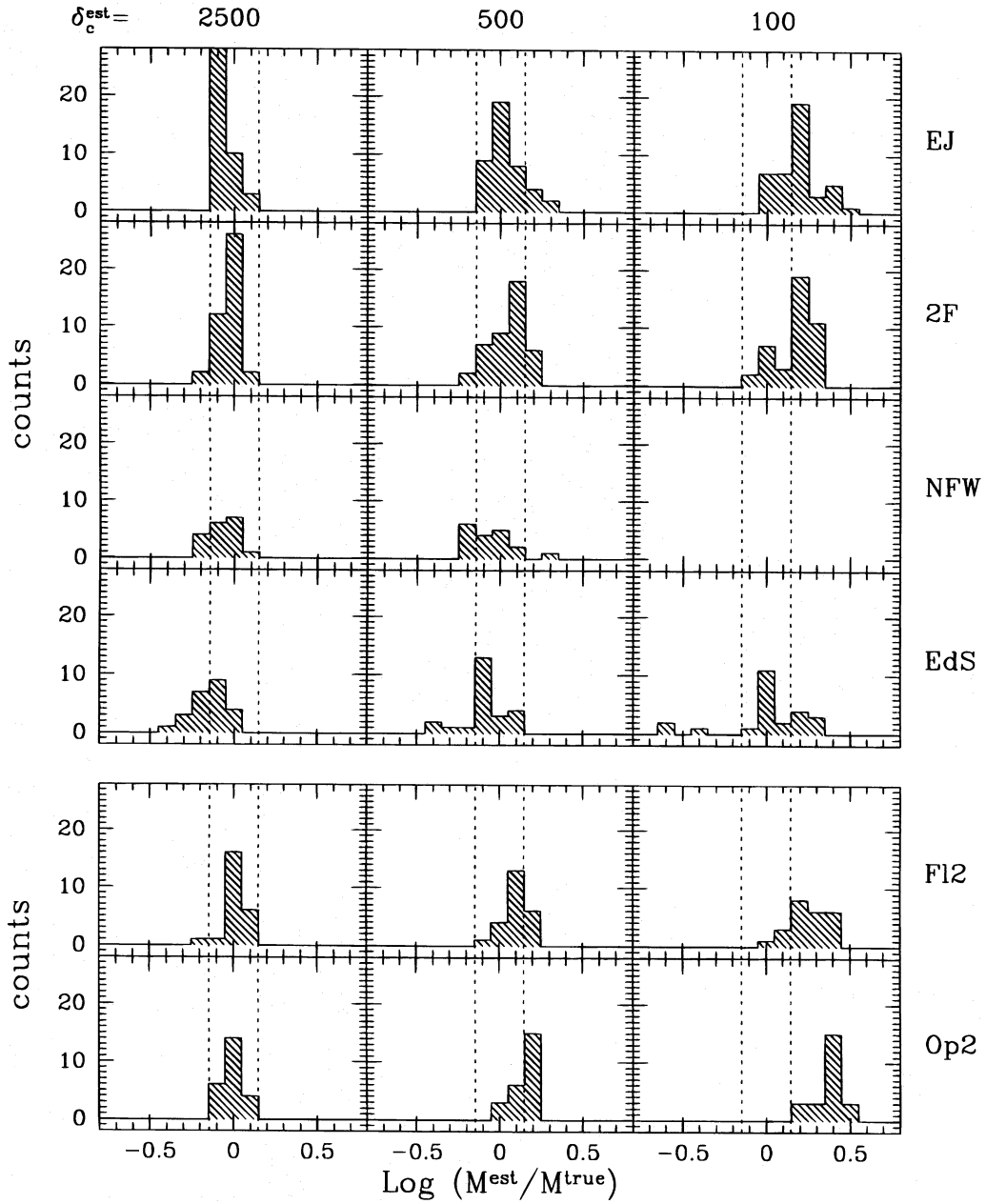

FIG. 7.—Histograms of the estimated-to-true mass ratios derived from the β-model evaluated at three different estimated density contrasts. Dashed vertical lines show an error of $\pm 40\%$.

TABLE 4

β-MODEL ACCURACY

	$\Omega = 1$		$\Omega_0 = 0.2$	
δ_c^{est}	$\bar{\mathscr{X}}^{a,b}$	$\sigma_{\mathscr{X}}$	$\bar{\mathscr{X}}^{a,b}$	$\sigma_{\mathscr{X}}$
100	1.46 (1.20)	0.53	2.08 (0.96)	0.50
250	1.15 (1.08)	0.36	1.60 (1.09)	0.33
500	1.02 (1.07)	0.29	1.34 (1.07)	0.24
1000.....	0.94 (1.00)	0.23	1.15 (0.99)	0.19
2500.....	0.87 (0.88)	0.16	1.00 (0.96)	0.14

[a] $\mathscr{X} \equiv M^{est}/M^{true}$.

[b] Numbers in parentheses include nonisothermal correction (see text).

is particularly important in the low Ω_0 ensemble because of their steeper temperature profiles.

Both the isothermal bias and the radial temperature correction are always smaller than 1 standard deviation in the $\Omega = 1$ mass estimates. The increase in the variance of $\mathscr{X}$ with radius in all models is presumably linked to the longer dynamical times of the outer regions. In the low-Ω_0 case, the bias in the isothermal estimates exceeds the scatter for $\delta_c^{est} \leq 500$, but the bias is removed by using radial temperature information. We expect that use of emission-weighted projected temperatures, rather than three-dimensional information, would change the correction factors $\mathscr{F}$ by $\lesssim 10\%$. Since instrumental and observing

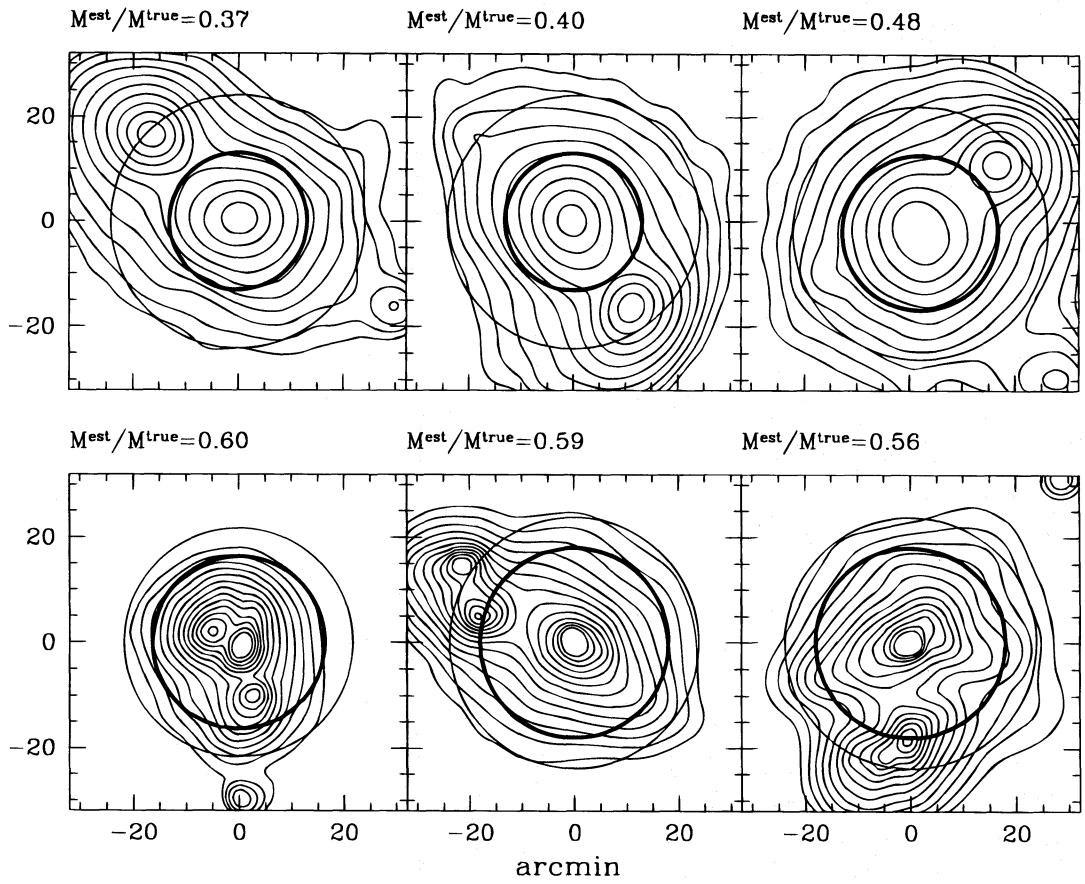

FIG. 8.—X-ray surface brightness maps of the six worst underestimates from the $\Omega = 1$ ensemble. Values of the estimated-to-true mass ratio are shown above each panel. Within each panel, the light and bold circles represent the true and estimated values of r_{500}, respectively. Strongly bimodal or complex images usually result in poor β-model mass estimates.

effects, particularly energy resolution and photon statistics, readily effect temperature estimates at this amplitude, we leave it for future, mission-specific modeling to investigate the correction factor using two-dimensional data.

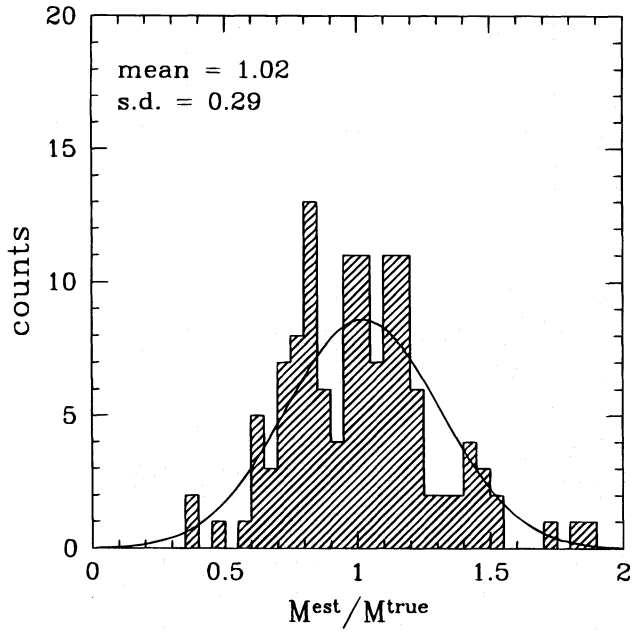

FIG. 9.—Histogram of the estimated-to-true mass ratios from the β-model for the $\Omega = 1$ combined sample at $\delta_c^{\rm est} = 500$.

Although the isothermal estimator fares worst in the case of strongly bimodal clusters (see Fig. 8), there are cases where the geometry of the projection, together with the interplay between the estimated values of β, r_c, and T_X, can result in accurate mass estimates even for clusters with suspicious-looking X-ray images. As an example, consider the cluster shown in Figure 1. The $\delta_c^{\rm est} = 500$ mass estimates for the three orthogonal projections yield (*from top to bottom*) $\mathscr{X} = 1.17$, 1.02, and 0.97. The most symmetric X-ray image incurs the largest error, while the two images displaying core bimodality are more accurately determined. Note that r_{500} for this cluster is 1.62 Mpc, or 24′ in the figure, well beyond the bimodal core. The larger value in the top projection compared to the others is due to slightly larger values of β and T_X and a smaller core radius compared to the other projections. These values result from the fact that the line of sight in the top panel is nearly parallel to the collision axis of the penetrating cores.

In summary, we find isothermal, β-model mass estimates to be nearly unbiased and accurate to a few tens of percents in the regime $250 \lesssim \delta_c^{\rm est} \lesssim 2500$ for the $\Omega = 1$ models and $\delta_c^{\rm est} \gtrsim 1000$ for the $\Omega_0 = 0.2$ sample. A bias toward overestimating masses exists at low values of $\delta_c^{\rm est}$. This bias, strongest in the low-Ω_0 models, can be eliminated by using radial temperature information instead of an isothermal assumption. Clusters with strongly bimodal or more complex images involve the largest mass underestimates. Because of the interplay of T_X, β, and r_c, there is not a simple, general connection between the properties of the

X-ray image and the accuracy of the mass estimates obtained with the β-model.

5. ESTIMATES BASED ON CLUSTER SCALING RELATIONS

As discussed in § 3.2, massive clusters within a given cosmology exhibit a remarkably similar structure when scaled to a fixed density contrast. Together with the condition of virial or hydrostatic equilibrium, this implies that the temperature of a cluster is, on its own, a good indicator of the size and mass of the system. Figure 4 shows this result very clearly. The tight correlation shown in this figure between T_X and r_{500} implies a similarly tight correlation between mass and temperature, since, by definition, the mean density within r_{500} is 500 times the critical density. Armed only with the broad-beam temperature measure T_X, we can thus form an estimate

$$M_{500}^{\rm est}(T_X) \equiv 500\,\frac{4\pi}{3}\,\rho_c(r_{500})^3 = 2.22\times 10^{15}\left(\frac{T_X}{10\ {\rm keV}}\right)^{3/2} M_\odot \qquad (8)$$

for the mass within the radius $r_{500}(T_X)$ given by equation (5).

We compare this mass estimate with the true mass within $r_{500}(T_X)$ for the $\Omega = 1$ ensemble in Figure 10. (Results for the $\Omega_0 = 0.2$ sets are similar.) The distribution of estimated-to-true mass ratios is nearly Gaussian, with a standard deviation of only 15%. Note that, in this case, no cluster in the $\Omega = 1$ sets has its mass over or underestimated by more than 40%, regardless of its dynamical state. This procedure can be extended to other values of the density contrast in a straightforward way. For a given δ_c, we compute the characteristic radii r_{δ_c} from the numerical sample and fit them to a relation of the form

$$r_{\delta_c}(T_X) = r_{10}(\delta_c)\left(\frac{T_X}{10\ {\rm keV}}\right)^{1/2}, \qquad (9)$$

where the normalization $r_{10}(\delta_c)$ is the average radial scale of 10 keV clusters at density contrast δ_c.

The resulting distributions of $\mathscr{X}$ are unbiased by construction and have standard deviation $\sigma_{\mathscr{X}}$. Table 5 shows the characteristic radii $r_{10}(\delta_c)$ and the scatter in the mass estimator $\sigma_{\mathscr{X}}$ for density contrasts $\delta_c = 100$, 250, 500, 1000, and 2500. Slight offsets in the characteristic radii are evident between the high and low-Ω cosmologies, consistent with the difference in cluster density profiles. As in the β-model estimates, the scatter in the mass estimates increases with radius. At density contrasts of a few thousand, the uncertainty in the mass estimates is extremely small, $\sigma_{\mathscr{X}} \lesssim 10\%$.

Another way to interpret these results is to consider that the scaling-law mass estimate is consistent with the hydrostatic, β-model estimate, equation (2), when evaluated at $r_{500}(T_X)$ with a characteristic value of β given by

$$\beta_* = 0.79[1 + (r_c/r)^2]\,. \qquad (10)$$

The second term is a typically small ($\lesssim 5\%$) correction at $\delta_c = 500$. This value for β compares well with measured values of β for many well-studied, rich X-ray clusters, among them Coma (Hughes 1989) and A2256 (Briel et al. 1992).

Why are the scaling-law estimates more accurate than those of the β-model? Consider the variance in the β-model mass estimated at a fixed radius:

$$\left(\frac{\Delta M}{M}\right)^2 = \left(\frac{\Delta T_X}{T_X}\right)^2 + \left(\frac{\Delta\beta}{\beta}\right)^2 + 2\left(\frac{\Delta T_X}{T_X}\,\frac{\Delta\beta}{\beta}\right). \qquad (11)$$

In a universe filled with perfectly hydrostatic, self-similar clusters, all clusters would follow a $r_{\delta_c}(T_X)$ relation like that in equation (9) exactly, and all would have a fixed value β_* for their outer profile slope. Introduction of perturbations in temperature and density off this perfect sequence will lead to a nonzero variance in the mass estimate. The only way to retain perfect mass estimates is to introduce anti-correlated perturbations $\Delta\beta/\beta \equiv -\Delta T_X/T_X$ in density and temperature, so that hydrostatic equilibrium is maintained. Uncorrelated perturbations in β and T_X will lead to a larger variance than that arising from perturbations in one parameter alone.

Figure 11 shows the perturbations measured directly in the simulations. Perturbations in β are defined with respect to the average, $\beta_* = 0.79$, while those in temperature are defined with respect to the mean radius-temperature relation, using the known value of r_{500} to define the unper-

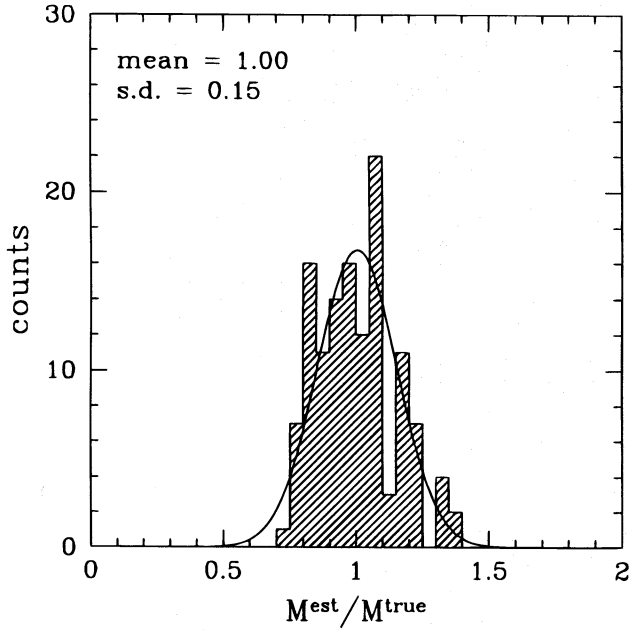

FIG. 10.—Histogram of the estimated-to-true mass ratios from the scaling-law method for the $\Omega = 1$ combined sample at $\delta_c = 500$. The distribution is unbiased by construction.

TABLE 5

SCALING-LAW ACCURACY

	$\Omega = 1$		$\Omega_0 = 0.2$	
δ_c	$r_{10}(\delta_c)^a$	$\sigma_{\mathscr{X}}$	$r_{10}(\delta_c)^a$	$\sigma_{\mathscr{X}}$
100	4.89	0.20	4.78	0.20
250	3.37	0.18	3.31	0.16
500	2.48	0.15	2.48	0.14
1000.....	1.79	0.11	1.87	0.12
2500.....	1.11	0.08	1.25	0.10

[a] Defined by eq. (9); units are Mpc ($h = 0.5$).

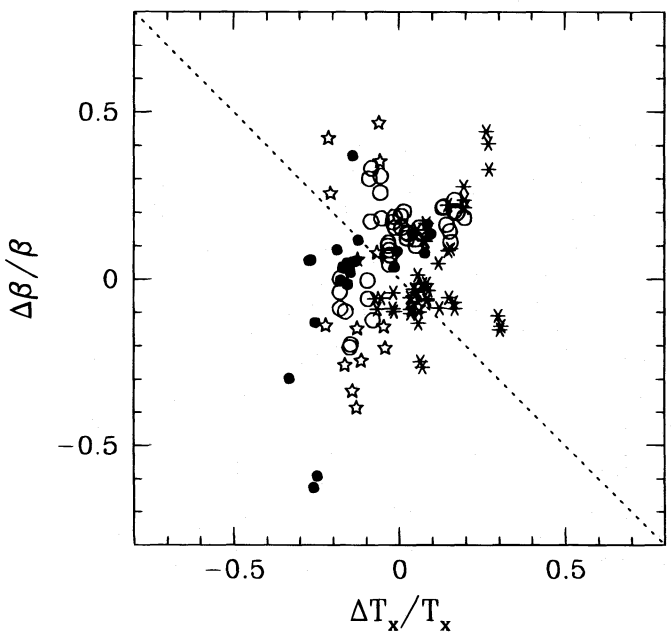

FIG. 11.—Scatter plot of the deviations in β and T_X (defined in the text) for all the models in the ensemble. Symbols are the same as those used in Fig. 4. Clusters in perfect hydrostatic equilibrium would display an anticorrelation (*dashed line*), which is not supported by the numerical data.

turbed cluster temperature for each cluster. It is clear from this figure that the data exhibit no anticorrelation between $\Delta\beta/\beta$ and $\Delta T_X/T_X$. The larger variance in the β-model compared to the scaling-law mass estimates can thus be understood as arising from an additional, independent source of error in the β-model estimator; *the introduction of β from X-ray imaging is essentially adding noise to the mass estimates.* As a concrete example, consider again the three images in Figure 1. The β-model mass estimates yield $\mathscr{X} = 1.17$, 1.02, and 0.97 (*from top to bottom*), whereas the scaling-law results are $\mathscr{X} = 1.05$, 1.00, and 0.99, respectively.

The "noise" added by the measured values of β has several sources. Recent dynamics play a role. Clusters are not in exact hydrostatic balance, particularly in their outer parts. The present density and temperature structure can be perturbed by prior mergers and accretion. Geometry also plays a role. The cluster gas distribution is, in general, ellipsoidal rather than spherical, and the measured values of β are obtained from projected, two-dimensional images of the three-dimensional density distribution. Finally, values of β derived from surface brightness fits are sensitive to contamination from foreground/background sources, choice of cluster center, and image quality and technical aspects of data reduction procedures. These concerns are compounded when one considers the basic fact that β is a measure of the *derivative* of the logarithm of the surface brightness.

The scaling-law method is superior to the β-model because of its smaller variance. Its accuracy is also remarkably insensitive to the dynamical state of clusters and the cosmological background. Its main drawback is the reliance on numerical experiments to provide the nomalization, $r_{10}(\delta_c)$, of equation (9), which, in turn, depends on the particular stucture formation model under scrutiny, and may depend as well on the numerical method used in the investigation. Regarding the latter, we are encouraged by the good agreement shown between two independent codes used in this study. We anticipate that future studies by groups employing independent numerical methods will address the robustness of the normalization $r_{10}(\delta_c)$. We also find room for optimism in the rather modest sensitivity to Ω_0 displayed by the normalization and scatter in mass estimates shown in Table 5. This insensitivity may be rooted in the fact that the scaling laws merely reflect the condition of virial equilibrium within $\delta_c \sim O(10^3)$. Overall, these results show that it is possible to use X-ray spectroscopy to estimate cluster masses with an rms accuracy substantially better than 20%.

6. DISCUSSION AND CONCLUSIONS

The results described in the previous sections agree well with those of Schindler (1996), who found biases and variance of a few tens of percents or less in the "normal cluster" sample derived from the numerical simulations of Schindler & Böhringer (1993) and Schindler & Müller (1993). The simulations and analysis methods in those works differ in many respects from those used here. In particular, the Eulerian gasdynamics scheme adopted in their study captures shocks more accurately than the SPH technique used here, while the adaptive nature of the SPH smoothing kernel provides better spatial and mass resolution in high-density regions. Given the significant differences between the independent simulation algorithms used in these studies, we find the degree of qualitative and quantitative agreement rather encouraging.

Tsai, Katz, & Bertschinger (1994) also examined the accuracy of the β-model mass estimates applied to an SPH simulation that included radiative cooling for the gas but excluded the effects of galaxy formation and feedback. At 1 Mpc from their cluster center, where $\delta_c \simeq 700$, they found that the β-model overestimated the mass by $\sim 25\%$, typical of the uncertainties found in our analysis. They also found large underestimates at radii near the core radii of their surface brightness fits (~ 200 kpc), which arose, in part, from the presence of a strong gradient in the gas temperature near the center. However, at these high density contrasts, their results are compromised by the artificially strong concentration of baryonic material near the center.

The improved variance of the scaling-law estimates over the β-model is a mixed blessing. A serious concern is the sensitivity of the slope and normalization of the r_{δ_c}-T_X relation to the assumed cluster physics and the underlying cosmological model. We find very modest sensitivity to Ω_0 near $\delta_c \simeq 10^3$ (Table 5) and find that the ejection models do not differ substantially from the infall sample. We suspect, and this suspicion is supported by collisionless simulations of cluster formation (Crone et al. 1994), that the impact of changing the initial perturbation spectrum will be less than that of varying Ω_0, but this issue remains to be investigated in detail.

What, then, should an observer with X-ray data do to estimate a cluster's mass? It depends on whether it is more important to minimize the bias or the variance in the mass estimate. For example, when comparing a set of X-ray–derived masses to values derived using an independent method (e.g., weak gravitational lensing), minimizing the bias in the X-ray binding masses would perhaps be most important, and the β-model approach would be preferred. On the other hand, if one were looking for the slope of

correlations between an observable cluster property (e.g., optical luminosity or velocity dispersion) and binding mass, then minimizing the variance would be more important and the scaling-law method preferred.

To summarize, we have used an ensemble of 58 gas-dynamic cluster simulations to investigate the accuracy of binding-mass estimates based on the hydrostatic, isothermal β-model and on the temperature-mass relation. We have also analyzed the velocity and temperature fields of the numerical models to address the questions of hydrostatic equilibrium and isothermality. A summary of our main results follows.

1. Within a radius, r_{500}, where the cluster mean interior density is 500 ρ_c, the gas velocity field is extremely quiet (Table 3 and Fig. 3), validating the basic assumption of hydrostatic support by thermal pressure, Despite local variations in temperature due to ongoing merger events (Fig. 1), the radially averaged gas temperatures are nearly isothermal within r_{500} in the $\Omega = 1$ sample. The $\Omega_0 = 0.2$ clusters exhibit stronger, negative radial temperature gradients.

2. The standard β-model mass estimator (eq. [4]) is nearly unbiased and has a modest scatter in regions where the mean estimated density contrast is in the range $500 \lesssim \delta_c^{\rm est} \lesssim 2500$. For example, at $\delta_c^{\rm est} = 1000$, the mean value of $M^{\rm est}/M^{\rm true}$ is 0.94 (1.15) with standard deviation 0.23 (0.19) for the $\Omega = 1$ ($\Omega_0 = 0.2$) sample. The bias and scatter both increase with cluster radius (decreasing δ_c), the former because the true density profiles are steeper than assumed and the latter because the dynamical time increases with radius. The bias can be removed by use of radial gas temperature profiles.

3. We find a strong correlation between r_{δ_c}, the radius encompassing a mean density contrast δ_c, and $T_{\rm X}$, the broad-beam, emission-weighted gas temperature. This scaling—a reflection of the similarity between clusters of different mass and their near-virial equilibrium state—can be used to generate mass estimates with smaller variance than that of the β-model. The degree of scatter is surprisingly small. At $\delta_c = 1000$, the standard deviation is 0.11 (0.12) for the $\Omega = 1$ ($\Omega_0 = 0.2$) sample. The larger dispersion in the β-model method arises because two parameters, β and $T_{\rm X}$, contribute independent sources of error, whereas the scaling-law method incurs error from only one parameter, $T_{\rm X}$.

The results from the experiments reported here and those from other experiments cited above practically rule out the possibility of large systematic errors in the mass determination of galaxy clusters. The large baryon fractions measured in clusters therefore remain difficult to reconcile with standard primordial nucleosynthesis in an $\Omega = 1$ universe.

This research was supported by NASA through grants NAGW-2367 and NAG 5-2790, by a NATO International Travel Grant, and by the NSF through grant PHY 94-07194. A. E. E. and J. F. N. are grateful for the hospitality provided by the ITP and UCSB during the Radiation Backgrounds and Galaxy Formation workshop and thank D. Bond, C. Norman, J. Ostriker, and S. White for their organizational efforts. C. A. M. acknowledges support from a Rackham Predoctoral Fellowship and a Sigma Xi Grant-In-Aid of Research at the University of Michigan, and the Department of Energy and NASA grant NAG 5-2788 at Fermilab.

REFERENCES

Bartelmann, M. 1995, A&A, 299, 11
Bartelmann, M., Steinmetz, M., & Weiss, A. 1995, A&A, 297, 1
Bartlett, J. G., Blanchard, A., & Silk, J. 1995, Science, 267, 980
Bertschinger, E. 1985, ApJS, 58, 39
———. 1987, ApJ, 323, L103
Bird, C. M. 1995, ApJ, 445, L81
Bonnet, H., Mellier, Y., & Fort, B. 1994, ApJ, 427, L83
Briel, U. G. & Henry, J. P. 1994, Nature, 372, 439
Briel, U. G., Henry, J. P., & Böhringer, H. 1992, A&A, 259, L31
Briel, U. G., et al. 1991, A&A, 246, L10
Buote, D. A., & Tsai, J. C. 1996, ApJ, 458, 27
Carr, B. 1993, Nature, 363, 16
Cavaliere, A., & Fusco-Femiano, R. 1976, A&A, 49, 137
Cen, R., & Ostriker, J. P. 1992, ApJ, 399, L113
Copi, C. J., Schramm, D. N., & Turner, M. S. 1995, Science, 267, 192
Crone, M. M., Evrard, A. E., & Richstone, D. O. 1994, ApJ, 434, 564
———. 1996, ApJ, in press
David, L. P., Jones, C., & Forman, W. 1995, ApJ, 445, 578
Dressler, A., & Shectman, S. A. 1988, AJ, 95, 985
Durret, F., Gerbal, D., Lachièze-Ray, G., Lima-Neto, G., & Sadat, R. 1994, A&A, 287, 733
Evrard, A. E. 1990, ApJ, 363, 349
Evrard, A. E., Mohr, J. J., Fabricant, D. G., & Geller, M. J. 1993, ApJ, 419, L9
Fahlman, G., Kaiser, N., Squires, G., & Woods, D. 1994, ApJ, 437, 56
Freedman, W., et al. 1994, Nature, 371, 757
Frenk, C. S., White, S. D. M., Efstathiou, G., & Davis, M. 1990, ApJ, 351, 10
Gunn, J. E., & Gott, J. R. 1972, ApJ, 209, 1
Hatta, N., Scherrer, R. J., Steigman, G., Thomas, D., & Walker, T. P. 1996, ApJ, 458, 637
Hoffman, Y. 1988, ApJ, 328, 489
Hughes, J. P. 1989, ApJ, 337, 21
Ikebe, Y., et al. 1994, in Clusters of Galaxies, ed. F. Durret, A. Mazure, & J. Tranh Thanh Van (Gif-sur-Yvette: Editions Frontières), 167
Krauss, L., & Kernan, P. J. 1994, ApJ, 432, L79
Loeb, A., & Mao, S. 1994, ApJ, 435, L109
Metzler, C. A. 1995, Ph.D. thesis, Univ. Michigan
Metzler, C. A., & Evrard, A. E. 1994, ApJ, 437, 564
———. 1996, in preparation
Miralde-Escudé, J., & Babul, A. 1995, ApJ, 449, 18
Miyaji, T., et al. 1993, ApJ, 419, 66
Mohr, J. J., Evrard, A. E., Fabricant, D. G., & Geller, M. J. 1995, ApJ, 447, 8
Mould, J., et al. 1995, ApJ, 449, 413
Mushotzky, R. 1994, in Clusters of Galaxies, ed. F. Durret, A. Mazure, & J. Tranh Thanh Van (Gif-sur-Yvette: Editions Frontières), 167
Navarro, J. F., Frenk, C. S., & White, S. D. M. 1995a, MNRAS, 275, 720
———. 1995b, ApJ, submitted
Navarro, J. F., & White, S. D. M. 1993, MNRAS, 265, 271
———. 1994, MNRAS, 267, 401
Neumann, D. M., & Böhringer, H. 1995, A&A, 301, 865
Pearce, F., Thomas, P. A., & Couchman, H. M. P. 1994, MNRAS, 268, 953
Pildis, R. A., Bregman, J. N., & Evrard, A. E. 1995, ApJ, 443, 514
Ponman, T. J., Allan, D. J., Jones, L. R., Merrifield, M., McHardy, I. M., Lehto, H. J., & Luppino, G. A. 1994, Nature, 369, 462
Rottgering, H., Snellen, I., Miley, G., DeJong, J. P., Hanisch, R. J., & Perley, R. 1994, ApJ, 436, 654
Sasselov, D., & Goldwirth, D. 1995, ApJ, 444, 5
Schindler, S. 1996, A&A, 305, 858
Schindler, S., & Böhringer, H. 1993, A&A, 269, 83
Schindler, S., & Müller 1993, A&A, 272, 137
Smail, I., Ellis, R. S., Fitchett, M. J., & Edge, A. C. 1995, MNRAS, 273, 277
Squires, G., Kaiser, N., Babul, A., Fahlman, G., Woods, D., Neumann, D., & Böhringer, H. 1995, preprint astro-pg/9507008
Steigman, G. 1995, in The Light Element Abundances, ed. P. Crane (Berlin: Springer), 109
Tsai, J. C., Katz, N., & Bertschinger, E. 1994, ApJ, 423, 553
Tyson, J. A., Valdes, F., & Wenk, R. A. 1990, ApJ, 349, L1
Walker, T. P., Steigman, G., Schramm, D. N., Olive, K. A., & Kang, H. 1991, ApJ, 376, 51
Watt, M. P., Ponman, T. J., Bertram, D., Eyles, C. J., Skinner, G. K., & Willmore, A. P. 1992, MNRAS, 258, 738
White, D. A., & Fabian, A. C. 1995, MNRAS, 273, 72
White, S. D. M., Navarro, J. F., Evrard, A. E., & Frenk, C. S. 1993, Nature, 366, 429